Article

Unified Framework for Ship Detection in Multi-Frequency SAR Images: A Demonstration with COSMO-SkyMed, Sentinel-1, and SAOCOM Data

Roberto Del Prete *, **Maria Daniela Graziano** and **Alfredo Renga**

Department of Industrial Engineering, University of Naples Federico II, P.le Tecchio 80, 80125 Naples, Italy
* Correspondence: roberto.delprete@unina.it; Tel.: +39-081-7682160

Abstract: In the framework of maritime surveillance, vessel detection techniques based on spaceborne synthetic aperture radar (SAR) images have promoted extensive applications for the effective understanding of unlawful activities at sea. This paper deals with this topic, presenting a novel approach that exploits a cascade application of a pre-screening algorithm and a discrimination phase. Pre-screening is based on a constant false alarm rate (CFAR) detector, whereas discrimination exploits sub-look analysis (SLA). For the first time, the method has been validated with experiments on multi-frequency (C-, X-, and L-band) SAR images, demonstrating a significant reduction of up to 40% in false alarms within highly congested scenarios, along with a notable enhancement of the receiving operating characteristic (ROC) curves. For future synergic exploitation of multiple SAR missions, the developed dataset, composed of Sentinel-1, SAOCOM, and COSMO-SkyMed images, is comprehensive, having images gathered over the same area with a short time lag (below 15 min). Finally, the diversified processing chains and the results for each mission product and scenario are discussed. Being the first dataset of single-look complex (SLC) SAR multi-frequency data, the present work intends to encourage additional investigation in this promising field of research.

1. Introduction

SAR data possess the potential to monitor various ocean surface features, such as ocean surface turbulence [1], including the detection of ship wakes [2–5]. Therefore, there is considerable interest in automatic ship detection in SAR images [6], which can provide quantifiable measurements of physical properties such as length and shape as well as dynamic movements such as speed and bearing. Notably, the detection of vessels can be attained both with airborne [7], spaceborne [8] and in situ instrumentation [9].

Concerning the latter, the Automatic Identification System (AIS), a very high-frequency (VHF) transceiver built originally for collision avoidance, is the most massive source of information used for maritime monitoring by Vessel Traffic Services (VTS) [10]. The broadcasted messages contain useful information about a vessel's identity, position, speed, course, destination, and other data that are critical for maritime control and navigational safety [11]. This critical information is delivered in a ship-to-ship and in a ship-to-shore fashion with transmissions to AIS stations (Figure 1).

The initial worries regarding the efficacy of an AIS-based monitoring system can emerge when examining its coverage at sea, which is up to 20 nautical miles without repeaters. However, the major issue with the AIS lies in its "cooperative" nature. The transmitter can be purposefully set off during unlawful activities. In such a circumstance, the ship becomes a "dark vessel" (i.e., a vessel that operates without an AIS transponder or with it turned off [12]). Still, the AIS legislation retains its carrying obligation only for certain classes of vessels. As stated in the SOLAS regulation [13], all passenger ships

(regardless of size), international voyaging ships of a gross tonnage (GT) of 300 or more, and 500 GT and greater cargo ships not embarked on international journeys are obliged by the International Maritime Organization (IMO) to be equipped with AIS [13]. Finally, situations of corrupted or incorrect AIS messages are prone to occur [14]. Therefore, while definitely contributing to maritime domain awareness (MDA), AIS information is unable to render the entire maritime picture. To actually be helpful, the AIS messages must be used in cooperation with other sensors, specifically non-cooperative ones that also show wider coverage [15]. Mainly for these reasons, satellite technologies are currently integrated into marine surveillance services and procedures because they provide cost-effective remote monitoring, a worldwide scope, regular updates, and a large volume of data gathered [11,16,17]. Even if optical imagers started gaining attention [16], spaceborne synthetic aperture radars (SARs) remain the most preferred choice because they offer unique characteristics that make them particularly tailored to supporting AIS-based monitoring systems. The SAR imaging mechanism exploits microwave pulses interacting with a target and returning to the sensor. Ships are usually man-made targets, making their backscattered energy significantly higher than the surrounding clutter. Therefore, a vessel usually appears as a cluster of bright pixels in an SAR image with few features that are identifiable. Notably, SAR is an active sensor not facing the disadvantage of operating only during the daytime. It is worth noting that most illegal activities take place at night. Moreover, the transmitted electromagnetic wave in the typical range of utilization (1–10 GHz) is not significantly affected by cloud cover or precipitation, thus making the imaging system able to penetrate clouds and detect vessels even during nighttime [18].
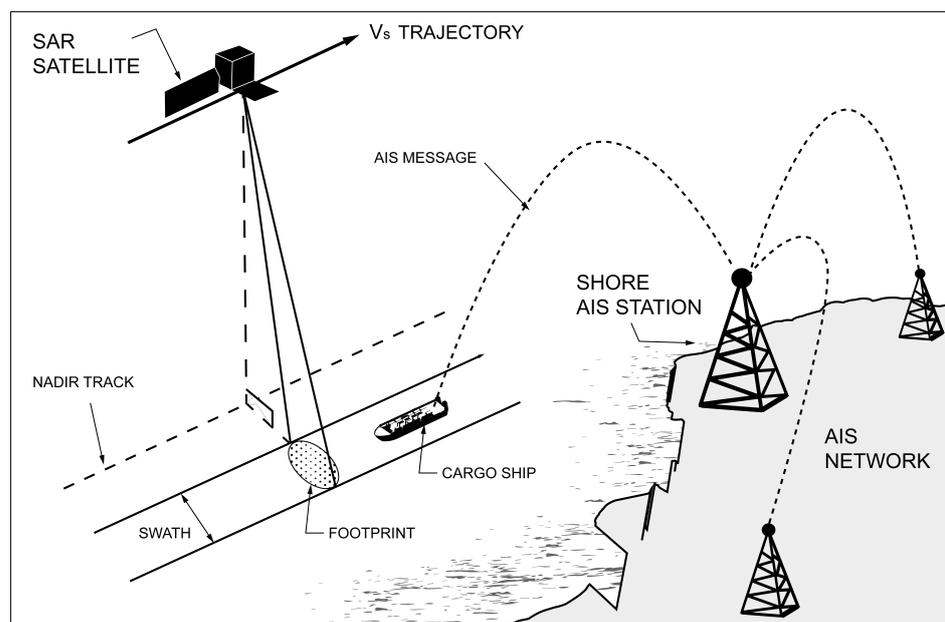

Figure 1. Pictorial view of a spaceborne SAR gathering an image over a coastal area.

For achieving effective maritime surveillance, not only the utilization of a non-cooperative approach but also the synergic exploitation of multi-frequency/multi-mission (MM/MF) data is essential. This is to take advantage of higher revisit times. This aim is approached by the present work through proposing a custom algorithm for ship detection adapted to three different SAR missions: Sentinel-1, SAOCOM, and COSMO-SkyMed. The algorithm uses the fast and efficient constant false alarm rate (CFAR) [19–22] together with the sub-look analysis (SLA) [23–26] discrimination technique. There is a wide corpus of research dealing with ship detection in SAR images, and the detection techniques in SAR imagery are influenced by several different key parameters, but the research on SAR ship detection can be divided into categories based on the physical property exploited. The backscatter-based methods [27,28] utilize the radar cross-sections (RCSs) [18] of the vessels. They

are fast and easy from a design point of view but have low performance, since they are typically affected by false alarms and ambiguities [24–26,29]. Polarization-based [26,30–34] approaches leverage the polarimetric scattering mechanism to separate ships from clutter. These approaches are generally more robust but are usually time-consuming and computationally intensive. That aside, for polarimetric scattering decomposition [35], quad-pol SAR imagery is required. The geometry-based methods [36,37] search for specific geometric features, such as the length, width, aspect ratio, perimeter, area, or contour. They demand an adequate template library and high-resolution SAR imagery. Feature-based methods use local feature descriptors (e.g., histograms of oriented gradients (HOG) [38], scale-invariant feature transform (SIFT) [39], and Haar-like features [40]). The methods show maturity in feature design, but they are time-consuming and weak in migration. Very recently, thanks to the large availability of Earth observation data, deep learning methods [41–47] were also introduced in the ship detection community. These techniques learn the non-hand-engineered abstract features from large annotated data for extrapolating specific patterns during inference time. Promising performance has been demonstrated even near coasts and reefs without the need for land separation [48]. The disadvantage of these methods is in the supervised learning approach that demands large labeled datasets.

As a further relevant aspect, it is important to acknowledge that the presence of sea clutter can have a significant impact on the detection of vessels in SAR imagery. The radar signal reflected by the sea surface is susceptible to scattering caused by minor fluctuations on the sea's surface, generating noise that can compromise the accuracy of statistical computations and produce false detections [49]. Various factors, including wind-generated waves, currents, and surface roughness, can trigger sea clutter, the manifestation of which is contingent on the SAR frequency and polarization, as well as the incidence angle and resolution of the sensor. To address the challenge of sea clutter in SAR imagery, the SLA approach can be employed to analyze pixel stability across the frequency spectrum. By using this approach, the effects of sea clutter can be mitigated, and the detection performance of vessels can be enhanced [23].

In the framework of the COastal Area monitoring with SAR data and multimission/multifrequency Techniques (COAST) project, funded by the Italian Space Agency (ASI), a novel dataset has been developed utilizing MM/MF imagery. The comprehensive dataset enables the testing of the effectiveness of several missions under comparable circumstances. To the knowledge of the authors, this constitutes the first single-look complex (SLC) MM/MF SAR dataset, and this is also a major novelty of this work. Another innovation lies in its specific attention to in-shore areas, which are typically characterized by perturbing phenomena affecting the detection performance. The latter can include the fast dynamics of vessels' motion near ports, ambiguities generated by land-strong scatterers, or saturation or anomalous side lobe pattern effects.

This manuscript is structured as follows. Section 2 details the development of the MM/MF SAR dataset and its ancillary information. Section 3 details the methodology adopted in this work from the pre-processing of the data to the implementation of a novel detector. Then, Section 4 discusses the results achieved by means of a large-scale validation approach on the proposed dataset. Finally, Section 5 draws the conclusions of the present study while also pointing out new future directions.

2. Multi-Mission/Multi-Frequency SAR Dataset

As stated above, for the construction of the MM/MF dataset, three missions were considered: the Italian COSMO-SkyMed (X-Band), the Argentinian SAOCOM (L-Band), and the European Sentinel-1 (C-Band). The characteristics of the selected products are briefly described in Table 1, which demonstrates how the images differ beyond the working frequency band. Concerning the Sentinel-1 images, they were gathered in dual-pol mode (VV + VH) or interferometric wide (IW) swath mode, even if VH-only data were processed. COSMO-SkyMed and SAOCOM were instead acquired in stripmap HH and VH polarization, respectively.

Table 1. MM/MF product specifications in terms of acquisition mode, pixel spacing, and polarization.

Mission	Acquisition Mode	Pixel Spacing (range × azi) (m)	Polarization	Swath (km)
COSMO-SkyMed	StripMap	0.5 × 0.5	HH	40
Sentinel-1	IW (Interferometric Wide Swath)	2.3 × 13.9	VH	250
SAOCOM	StripMap	<10 × 10	VH	65

2.1. Selected Scenarios

Data collection started from the selection and identification of the region of interest. For the present study, three different scenarios were selected for the purpose of maritime monitoring: Adriatic Sea, Sardinia, and the Egadi Islands (Figure 2).
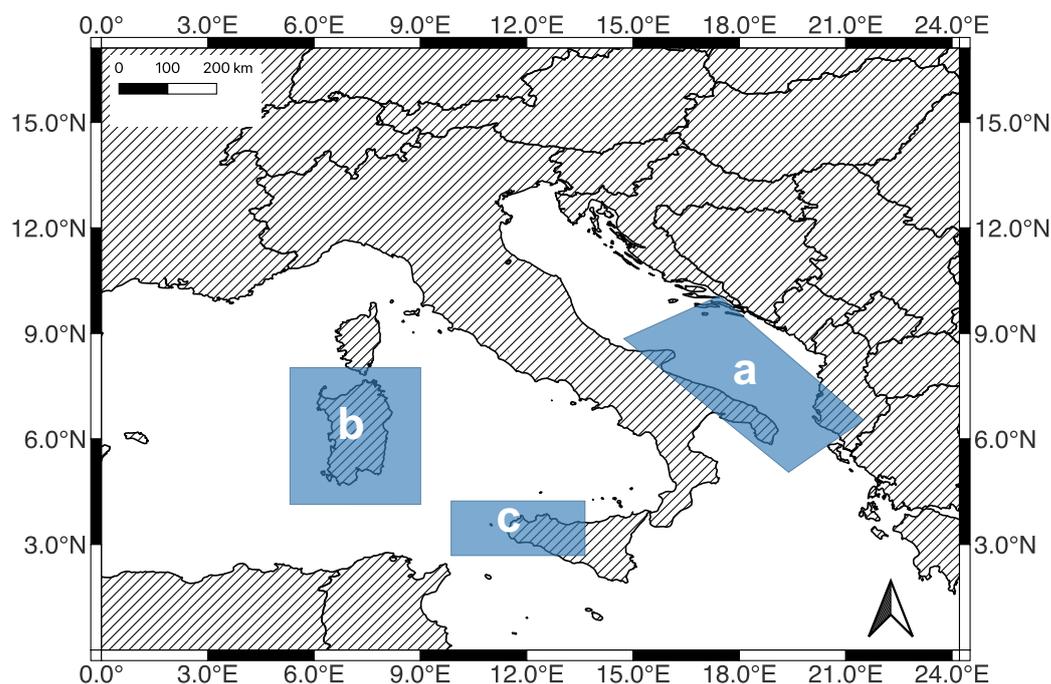

Figure 2. Selected scenarios of interest for the realization of the MM/MF dataset: (a) Adriatic Sea, (b) Sardinia, and (c) the Egadi Islands.

It must be emphasized once more that the goal was to maximize the benefits of MM/MF SAR images for maritime surveillance. As a result, a short time gap between successive acquisitions over the same region was required. A tool that inspected the effective spatial and temporal couplings of the MM/MF products was developed specifically for this purpose. The tool provides highlights of the various acquisition availabilities, reporting useful insights about the three SAR missions under consideration. Finally, the value of the project's supplementary AIS data was explored.

The Egadi Islands Marine Reserve, with its 53,992 hectares, is not only Europe's largest, but it also has the peculiarity of being the initial point of arrival for several marine species whose migrations are frequently linked to the flow of the Atlantic current. In recent years, there have been several complaints about illegal activities in the Egadi Islands' marine protected area, such as trawling in shallow waters or the use of illegal nets longer than the 2.5 km required by law for underwater fishing in prohibited areas [50]. Sardinia's scenario concerns violations related to the "waste cycle" and polluting discharge. In recent years, there have also been several seizures of drugs and weapons in Sardinian ports and waters. Additionally, according to recent research [51,52], Sardinia has the absolute record of seized fish products. Finally, in the Adriatic Sea, in general, there has been a drastic decline in fish

stocks due to intensive fishing, which has profoundly changed the marine environment. This is an area where excessive trawling has had a very strong impact, so much so that fish stocks in the Adriatic Sea have been greatly reduced [53]. Illegal fishing is not the only unlawful activity, as arms and drug trafficking and smuggling are also widespread.

2.2. Footprint Matching

The footprint matching algorithm (Algorithm 1) is a novel contribution of this paper that oversees coupling different SAR products on the same spot and proceeds in two cascaded steps. In the first stage, SAR products are filtered on a temporal basis, considering two products matched if their sensing period difference is below 15 min. This key value was determined with a heuristic rationale, whereby ships after that time difference could not be matched between the images. The algorithm serves as a pre-screening step and is followed by spatial matching to filter the product that covers the same area of interest (AOI). The spatial matching is carried out by exploiting the footprint data contained in the product metadata. The area of intersection is used to establish a correct spatial match between two footprints. Finally, to conclude the analysis, a visual inspection is performed. The footprints are plotted in interactive *.html maps, and the quality of the intersection is evaluated both in terms of area covered and area of interest, verifying that the intersections cover sea zones.

Algorithm 1: Footprint matching MM/MF SAR products.

Input: MM/MF Products
for each product p_i **do**
    for each product p_j with $j > i$ **do**
        if $|t_i - t_j| < 15$ **then**
            if p_i and p_j cover the same area of interest **then**
                $matchedProducts \leftarrow matchedProducts \cup (p_i, p_j)$;
return $matchedProducts$;

An example of a map realized for the scenario of Egadi Island is reported in Figure 3, with which it is possible to observe the Sentinel-1 and COSMO-SkyMed coupling.
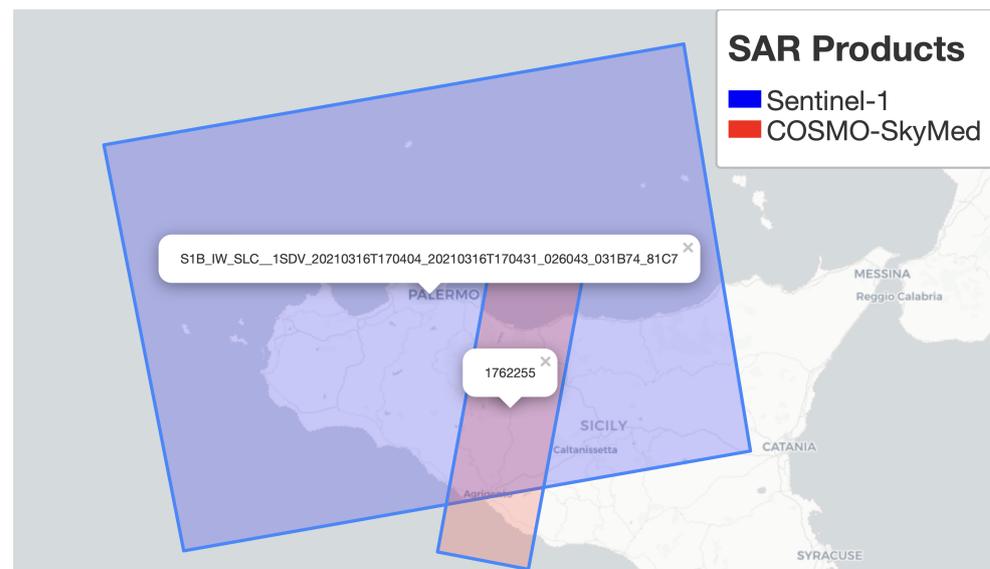

Figure 3. Sentinel-1 (Prod ID: *S1B_W_SLC_1SDV_20210316T170404_20210316T170431_026043_031B74_81C7*) and COSMO-SkyMed (Prod ID: *1762255*) product pairing map in the Egadi Islands scenario.

Table 2 shows the number of couplings in each scenario selected for the COAST project, detailing separately the various SAR mission parings. Notably, in the Egadi Islands

region, only the COSMO-SkyMed and Sentinel-1 products found matches. For major details regarding the coupled products, their relative geometries, orbit types, and platforms can be found in [54].

Table 2. Number of couplings for each scenario of interest of the MM/MF dataset.

Pairing / Region	Adriatic Sea	Egadi Islands	Sardinia
COSMO-SkyMed and Sentinel-1	15	32	55
COSMO-SkyMed and SAOCOM	5	NA	23
Sentinel-1 and SAOCOM	12	NA	10

2.3. AIS Data

Ancillary AIS data are a useful resource included in the dataset to provide information on specific targets. The AIS messages can be categorized into three types: static, dynamic, and voyage-related information. Only the dynamic one was updated frequently (<10 min), with a rate changing according to the vessel speed and course variation, ranging from a few seconds for very fast ships to several minutes for slow or moored ships. When collaborative ships were available, their position, contained in the SAR products, was stored in a database. Nonetheless, the storage policy of [55] saves the messages with a temporal resolution of around 1 min. Therefore, data were pre-processed beforehand, with Hermite interpolation taking as a reference time the central time of acquisition of each SAR image. Aside from that, when an insufficient number of points made it infeasible to execute an interpolation, an extrapolation technique was used. However, in many cases, this approach resulted in wrong placement of the ship location. This misleading result was caused by wrong extrapolation, erroneous AIS messages, or sudden route changes of the ships. Hence, the actual positions of ships were collected by visually inspecting each SAR image and manually labeling each vessel.

3. Method

The targets that are not truthful vessels acting as powerful signature ghosts are labeled as ambiguities in the SAR literature [23]. The method developed in this manuscript aims at mainly filtering the latter. The causes of ambiguities may be traced back to the limited sampling of the SAR pulses, which affects the Doppler spectrum [25]. Generally, SAR ambiguities can be produced in two ways. In the first case, the ambiguities are brought on by large ships. In this scenario, the ship's brightness creates ambiguity that may be stronger than the surrounding clutter, which might cause ghosts in the SAR picture to resemble the ship's actual signature. In the second case, the ambiguities are caused by land targets. Due to the low backscattering from the water in this scenario, which is a characteristic of coastal zones, the ambiguities produced by land targets are shown as bright targets over the sea's surface. In the case of high-resolution SAR images, these artifacts become more prominent. In essence, as the spatial resolution grows, so does the compression gain in SAR image formation. As a result, the improvement of the dynamic range of SAR images increases the intensity of strong point scatterers. The following sections describe in detail the pre-processing chains for each SAR product and the CFAR+SLA detector.

3.1. Pre-Processing Chains

A general understanding of the pre-processing chains implemented for the detection of visible ships in the MM/MF products is illustrated in Table 3, where each pre-processing step applied to the different SAR products is detailed with a checkmark. Sea-land segmentation is a mandatory step that can greatly minimize false alarm rates and enhance follow-up processing efficiency.

Table 3. Pre-processing operators used for each SAR product.

Product Operator	COSMO-SkyMed	SAOCOM	Sentinel-1
Multilook	✓		
Thermal noise removal			✓
TOPSAR deburst	✓		✓
Land masking	✓	✓	✓
Calibration	✓		✓

As also exhibited in Table 3, apart from land masking (LM) processing, SAOCOM products do not require any further dispensation. The multilook operator, applied only on COSMO-SkyMed products, is not mandatory but suggested to reduce the computational burden. Significant concerns regard the LM operator, which usually requires an accurate model of the coastline, whereas other researchers prefer to use specific extraction techniques [56]. In this paper, the land polygons were extracted from [57].

3.2. The CFAR+SLA Detector

The methodology developed proceeds in two steps in cascade: pre-screening and discrimination. First, the target proposals are generated with a traditional CFAR algorithm, and then these ones are discriminated with a spectrum analysis technique (i.e., sub-look analysis (SLA)). The adaptive threshold applied uses the nested windows approach, in which there are three windows around each pixel under testing: a target window (TW), a guard window (GW), and a background window (BW). The adaptive threshold is the basis of the pre-screening process. The size of the target window should be approximately equal to the size of the smallest object to detect, the size of the guard window should be approximately equal to the size of the largest object, and the size of the background window should be sufficiently large to estimate the local background statistics accurately. Indeed, the algorithm leverages the statistical modeling of the background clutter [58–61], with which a probability density function $f_{pdf}(x)$ can be associated. Thus, the design parameter T can be computed by the from user-selected *PFA* as follows:

$$PFA = 1 - \int_{-\infty}^{T} f_{pdf}(x)dx = \int_{T}^{\infty} f_{pdf}(x)dx. \tag{1}$$

It is worth highlighting that the T threshold is established empirically during practical implementation, with formulas solely serving as a directional guide. This is because a sufficiently accurate but also general enough model for the sea background is not typically available. Once the prompted background mean μ_b and standard deviation σ_b use pixels in the background ring and the mean value μ_t of the target window, a region is a potential target candidate if

$$\mu_t > \mu_b + \sigma_b * T. \tag{2}$$

Based on the output of Equation (2), the algorithm first groups the contiguous detected pixels into a single cluster and then extracts the width and length information from the clusters. Finally, clusters that are too large or too small are excluded based on these measurements and user input discrimination criteria. This first level of filtering is called geometric discrimination. In conclusion, CFAR detection is designed to search for pixels that are unexpectedly bright in comparison with those in the surrounding sea, although SAR ambiguities or sea clutter may also fit this criterion. The pseudo-code of the CFAR algorithm is reported in Algorithm 2.

Algorithm 2: CFAR algorithm.

Input: data, background, guard, and target window size, threshold T

Step 0: Raster Tiling input data (1px stride);

for each tile **do**

   1: Using the nested windows: background, guard, and target window:

      1.1 Calculate the average value of the background window;
      1.2 Calculate the standard deviation of the background window;
      1.3 Calculate the average value of the target window;

   2: Use Equation (2):

      if True

         then *Targets ← Targets ∪ newTarget*;

   3: Cluster continuous pixels marked as target;

      3.1 Apply Geometric Discrimination;

return *Targets*

To tackle the false alarm issue, the second level of discrimination employs sub-look analysis of the selected region of interest for the removal of false alarms. The physical rationale is that the Doppler spectra of ambiguities and targets are distinguished. As shown in Figure 4, subsets and metadata are fed as input to the SLA algorithm. The typical metadata information required by the sub-look processor contains parameters such as the pulse repetition frequency (PRF) or the bandwidth of processing in the azimuth [23].
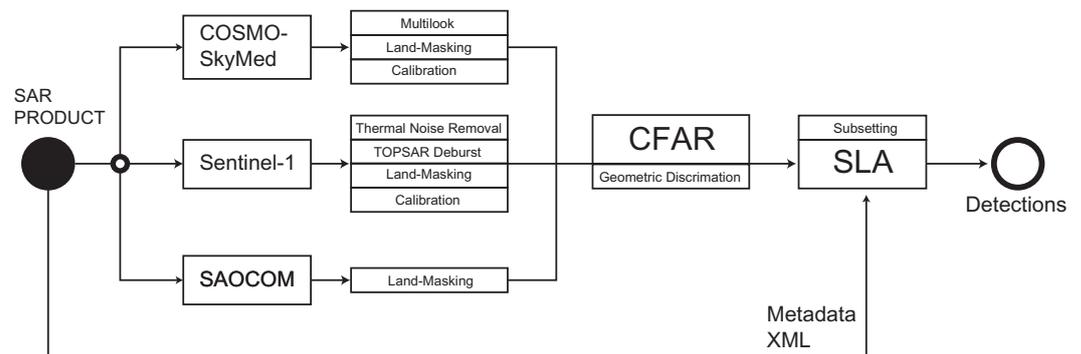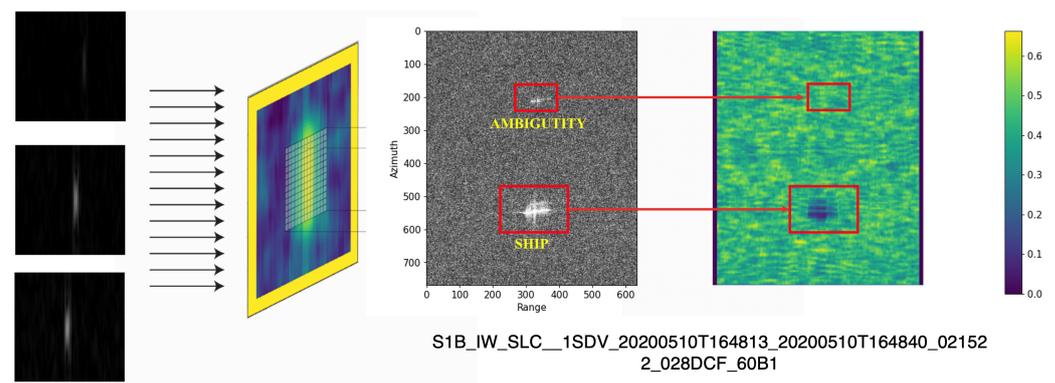

Figure 4. Complete processing flow of the CFAR and SLA algorithms.

Sub-looks are generated starting from the SLC regions of interests detected in the previous steps. As detailed in [23], one-dimensional sub-look generation is conceived, which is the most common approach for ship detection. Therefore, sub-looks can be generated either in the azimuth or in a range. It is worth recalling that there is no significant difference in ship detection performance between the range and azimuth sub-looks even when moving ships are imaged, but azimuth sub-looks are used in this work for ambiguity rejection. The number of sub-looks N_{SL}, the bandwidth of the sub-looks B_{SL}, and the frequency separation between the centroids of two close looks f_c constitute the relevant parameters that must be set. In general, B_{SL} is equally configured for all sub-looks. This ensures dealing with sub-looks having the same resolution and thus allowing a fair comparison between them. Indeed, the fraction of B_{SL} covered by a sub-look is an index of the degradation of the resolution with reference to the original resolution of the SLC data. Regarding N_{SL}, for ship detection purposes, usually only two sub-looks are considered. However, for estimating the incoherent entropy (IE) [23], a minimum of three sub-looks was used. Concerning the location of each sub-look, the common approach is to consider the sub-looks as equally spaced along the available bandwidth. It is worth remembering that sub-looks are overlapped in frequency if $f_c < B_{SL}$. Table 4 displays the parameters used for the sub-look analysis of Sentinel-1, COSMO-SkyMed, and SAOCOM missions.
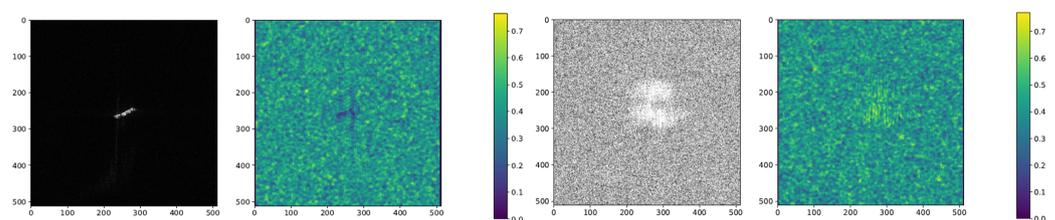
Table 4. Parametersused for the sub-look analysis of Sentinel-1, COSMO-SkyMed, and SAOCOM missions.

Mission Parameter	Sentinel-1	COSMO-SkyMed	SAOCOM
B_{SL}	102.0 Hz	466.6 Hz	372.0 Hz
f_c	102.0 Hz	466.6 Hz	372.0 Hz
W_r, W_c	7, 17	17, 17	3, 17

After sub-look generation, the IE relative to each region of interest was prompted. In the end, a threshold algorithm was applied by considering stable pixels in a nested window fashion. In fact, considering a matrix of IE prompted for a subset, a statistical process analyzed the average values inside and outside the small 30×30 pixel region at the center of each subset (Figure 5). As for the CFAR, a buffer window of 70×70 pixels was considered to reduce disturbances in the computations. To summarize, the discrimination algorithm output a class for the target or ambiguity depending on the stability of the pixels of the target, with reference to the pixel stability of the background. In conclusion, the CFAR+SLA detector can be considered an extension of [23], where the IE pertained only to the pre-screened targets and the thresholds were prompted in a nested fashion.

S1B_IW_SLC__1SDV_20200510T164813_20200510T164840_021522_028DCF_60B1

Figure 5. Visual representation of IE generation from three sub-looks (**left**) and its calculation for a Sentinel-1 product (**right**), in which a target and its ambiguity are highlighted.

Some demonstrative examples of IE for the COSMO-SkyMed, Sentinel-1, and SAOCOM ship targets and ambiguities are reported in Figures 6–8, respectively. These samples are very useful for showing the crucial behaviors of IE under different frequency bands while still not damaging the effectiveness of the discriminator.

Figure 6. Example of IE calculated for ship target (**left**) and ambiguity (**right**) for a CSK product. (Product ID: *CSKS1_SCS_B_HI_05_HH_RD_SF*_20201017164505_20201017164512).
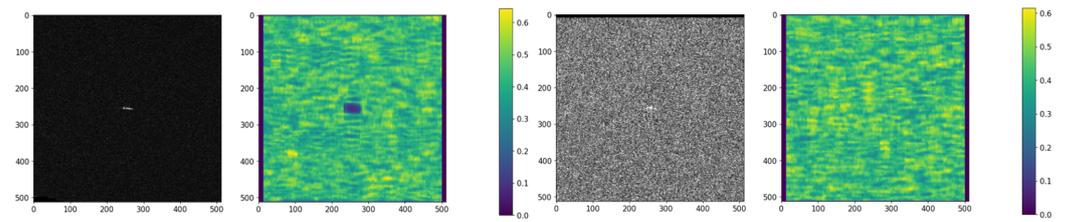
Figure 7. Example of IE calculated for ship target (**left**) and ambiguity (**right**) for a Sentinel-1 product. (Product ID: $S1B\_IW\_SLC\_\_1SDV\_20200510T164813\_20200510T164840\_021522\_028DCF\_60B1$).
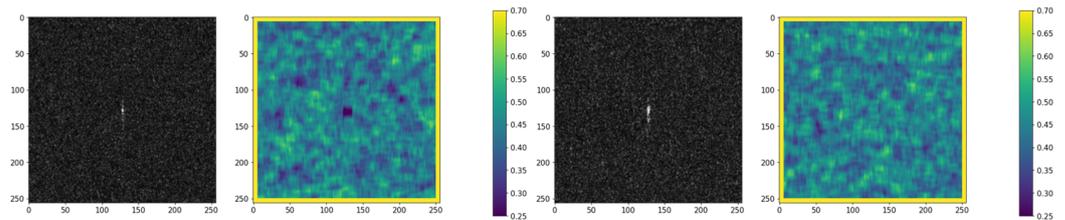

Figure 8. Example of IE calculated for ship target (**left**) and ambiguity (**right**) for a SAOCOM product. (Product ID: $S1A\_OPER\_SAR\_EOSSP\_\_CORE\_L1A\_OLVF\_20210122T210006$).

4. Experimental Analysis

4.1. Performance Indicators

To monitor the overall performance of the detection algorithm, the detection probability, false alarm rate, and consequently the receiver operating characteristic (ROC) curves were defined. It should be noted that in the literature, the metrics of the detection probability P_d and false alarm probability P_f are defined differently from author to author [62]. For example, some authors prefer to relate the false alarm rate to the area of the observation scenario [27]. In this study, such metrics were adopted as follows:

$$P_d = \frac{N_{dt}}{N_t} \qquad\qquad P_f = \frac{N_{Det} - N_{dt}}{N_{Det}} \qquad\qquad (3)$$

having denoted N_{dt} as the number of target-coupled detections, N_t as the number of targets in the scene, and N_{Det} as the total number of detection algorithm outputs. Once the metrics are defined, it is possible to measure the relative importance of the CFAR algorithm parameters for the detection performance. It is noteworthy that, having defined the metrics in such a way, the probability of detection and false alarm rate results are decoupled. However, before calculating these curves, an attempt was made to solve one of the issues of this adaptive threshold approach. While the CFAR algorithm is well-established and widely accepted in the scientific community, it is not without its faults. The multiple detections of the same target represent one of the most typical examples. To address this issue and consequently minimize the false alarm rate, a detection suppression technique was developed, combining nearby detections that are located less than 150 m apart from each other. The new location is supposed to be placed in the middle of the two. Notably, the threshold was experimentally determined.

4.2. Local Analysis

A study of the CFAR+SLA algorithm's performance on a COSMO-SkyMed product (Figure 9) is presented here.

This scene was chosen for its unique characteristics since it represents a very difficult case with intricate coasts, azimuth ambiguities, and ships in close proximity to one another and the coast. In fact, the image includes the port of Taranto, which features many potential sources of false alarms due to its geographical configuration. The presence of docks and other metal buildings is a further source of uncertainty. Finally, there is an artifact in the image, specifically a bright stripe, which is most likely the result of a radio signal emitted

by one of the ships in port and captured by the X-band satellite. The product was tested with a low threshold value, background, guard, and target window sizes as given in Table 5. In particular, the threshold value was computed by taking the value provided in Table 5 and converting it into a decimal fraction using the negative exponent of 10.

Figure 9. Test case of the CFAR+SLA algorithm over the port of Taranto. Highlighted detail: a probable radio signal transmitted from a ship and captured by X-band spaceborne SAR. Product ID: *CSKS*1_*SCS*_*BH1*_*05*_*HH*_*RD*_*SF*_20200323164522_2020032316_4529, processed by University of Naples Federico II under the COAST license of the Italian Space Agency (ASI). Original COSMO-SkyMed Product ©ASI (2020).

Table 5. Configuration of the paramaters of the CFAR algorithm.

BW	GW	TW	PFA (10^{-x})	Min Target Size	Max Target Size
800 m	400 m	30 m	4.5	30 m	800 m

This is the default option for running the algorithm in order to increase the detection probability while decreasing the false alarm rate. In any event, this permits the discrimination algorithm's performance to be tested across a large number of detections. The overall accuracy of the CFAR+SLA algorithm was evaluated through ship and ambiguity detection, having defined the accuracy as the ratio between the true positives and true positives plus false positives. Ultimately, pre- and post-application results of the discrimination chain were evaluated in terms of the detection probability and false alarm rate. The results were obtained and reported in Table 6.

Table 6. Accuracy of the CFAR+SLA algorithm and performance in terms of probability of detection and false alarm rate pre- and post-application of the discrimination pipeline.

	Accuracy	CFAR		CFAR+SLA	
Vessels	92.3%	P_d	P_f	P_d	P_f
Ambiguities	100%				
Global	95.6%	100%	47.8%	100%	7.6%

4.3. Global Analysis

This section details the performance analysis to estimate the improvement achieved with the CFAR-SLA algorithm with respect to the application of CFAR only. For this purpose, MM/MF products coupled by spatio-temporal matching were analyzed with the CFAR-SLA algorithm in the different identified regions. In more detail, after labeling the products individually, the performance was derived via ROC curves. What follows is a brief description of the curves obtained in each reference scenario. Since the AIS data were not fully usable, it should be noted that the goodness of the curves depended on the annotator's recognition skill. The ROC curves were calculated by varying the threshold parameters of the detection algorithm and keeping the other parameters fixed, as in the basic configuration shown in Table 5. Specifically, the threshold was linearly sampled in the interval [4.5, 19.25].

4.3.1. Egadi Islands

In the Egadi Islands region, the performance of the algorithm is highlighted in Figure 10. It should be taken into account that in this region, the land portions are far smaller than the sea portions. This made it possible to reduce the false alarm rate generated by land ambiguities. As can be seen from the results, the performances of Cosmo-SkyMed and Sentinel-1 were remarkable. Specifically, measuring the performance as the area under the curve (AUC), COSMO-SkyMed achieved a value of 0.91 with CFAR only, which increased to 0.95 after the the application of the discrimination pipeline. Concerning Sentinel-1 products, the AUC improved by more than 15% before and after application of the discrimination algorithm, going from 0.60 to 0.70.
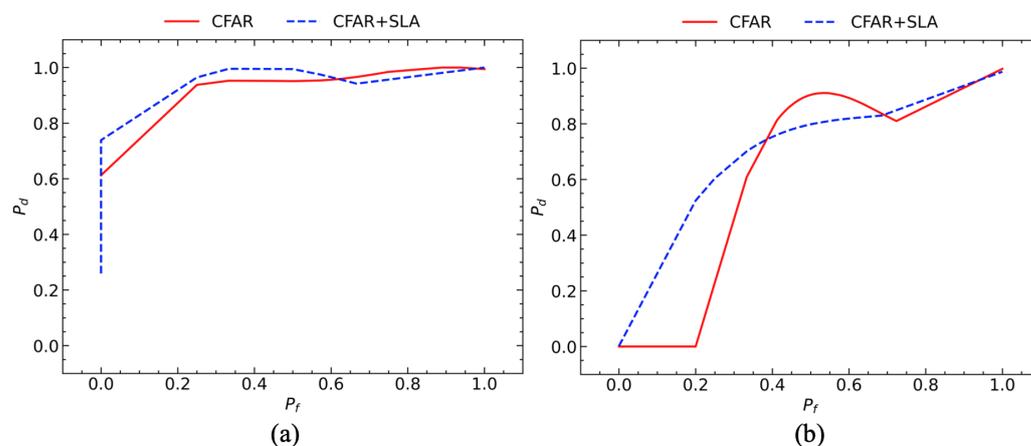

Figure 10. ROC evaluation of Cosmo-SkyMed (89 targets labeled) (**a**) and Sentinel-1 (290 targets labeled) (**b**) products in the Egadi Islands region.

4.3.2. Sardinia

The evidence of Figure 11 shows how the performance achieved in the region of Sardinia is noteworthy, proving the effectiveness of the discrimination algorithm.

Indeed, the COSMO-SkyMed products clearly demonstrate performance improvements. As can be seen, albeit with a marginal loss in accuracy in the early part of the graph, the COSMO-SkyMed products experienced a performance increase from the already high AUC value of 0.88 to 0.91. By observing Figure 11b, the SAOCOM products showed a small decay in the CFAR-SLA curve around the 0.7 value of Pf. However, as can be appreciated, the AUC markedly increased from a value of 0.78 to 0.82. The Sentinel-1 products (Figure 11) demonstrated good performance, which increased again using the sub-aperture algorithm. In fact, the performance enhancement increased the AUC from 0.72 to 0.77.
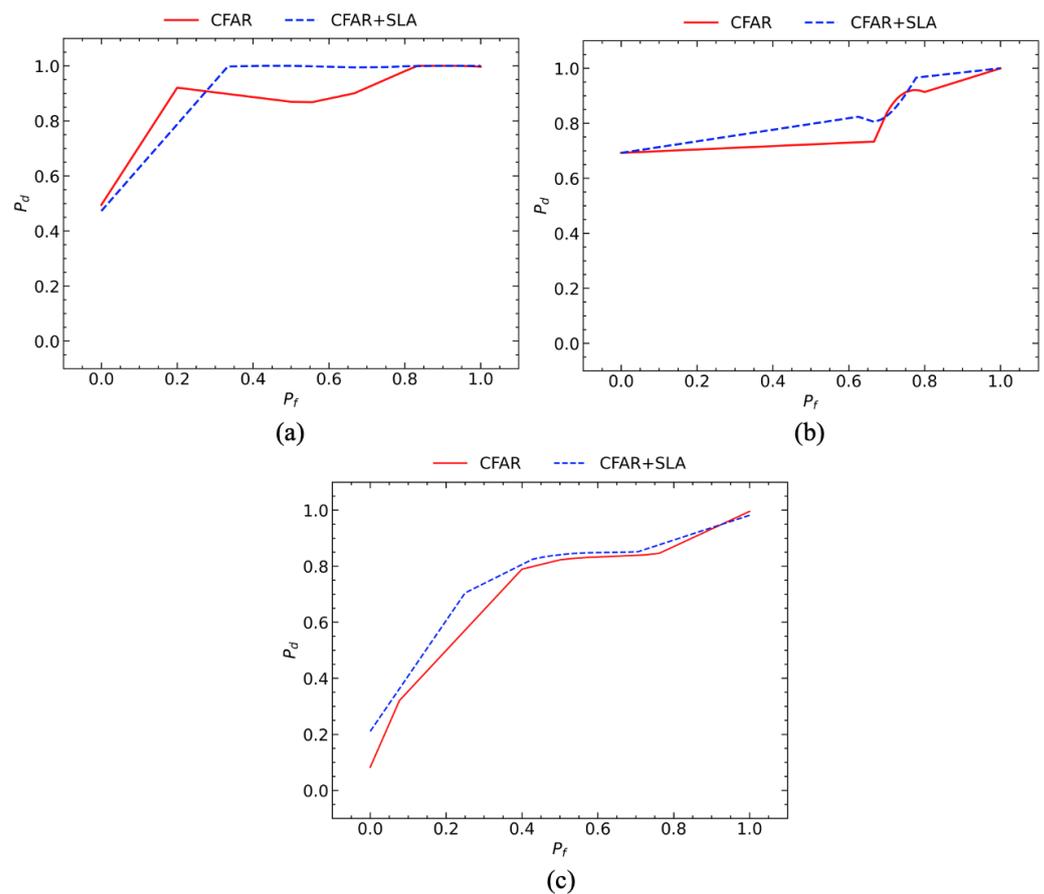
Figure 11. ROC evaluation of COSMO-SkyMed (121 targets labeled) (**a**), SAOCOM (36 targets labeled) (**b**), and Sentinel-1 (333 targets labeled) (**c**) products in the Sardinia region.

4.3.3. Adriatic Sea

When analyzing the products in the Adriatic Sea, it is again clear from the results obtained that there was an increase in performance after the removal of false alarms. The relevant curves can be seen in the graphs in Figure 12. In contrast to the previous case, the COSMO-SkyMed products showed a performance increase, especially in the early part of the graph. The accuracies were also remarkable in this scenario, going from a value of 0.78 to 0.87 for the AUC. The same observations can also be repeated for the SAOCOM products (Figure 12), showing an increased AUC after application of the discriminator algorithm. As can be seen from the bottom graph in Figure 12, the AUC increased from a value of 0.73 to 0.77. Finally, despite slightly lower accuracy values at the end of the graph, the Sentinel-1 products showed an improvement in detection performance, as the area under the curve improved from 0.83 to 0.88.

4.3.4. Area under the Curve

In essence, the global performance of the COSMO-SkyMed and Sentinel-1 as well as the COSMO-SkyMed and SAOCOM pairs were evaluated and reported by means of Figure 13. The latter reported the AUC before and after application of the sub-aperture analysis algorithm, divided into the three scenarios of interest. As can be seen from the graphs, the COSMO-SkyMed performance was remarkable in every scenario and condition, especially in the Egadi Islands region, where large portions of the sea overlie the few areas of land. This again testifies to the importance of the correct execution of land separation.
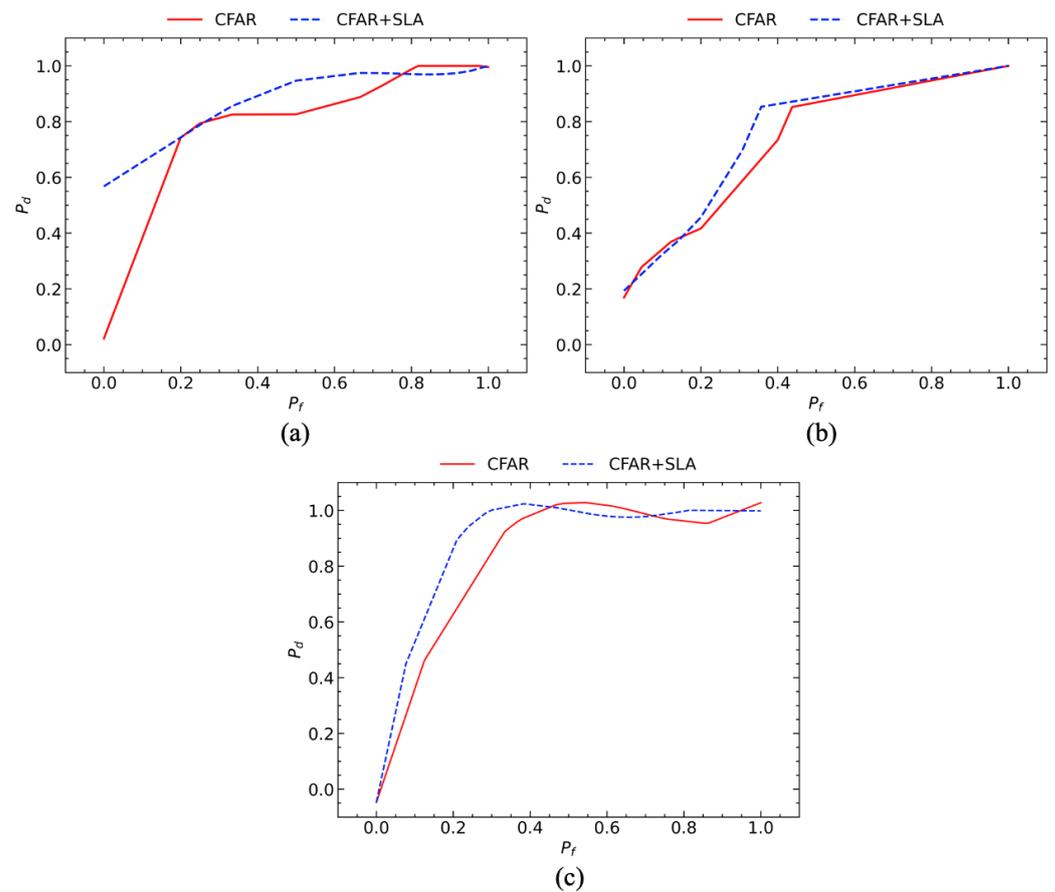
Figure 12. ROC evaluation of Cosmo-SkyMed (108 targets labeled) (**a**), SAOCOM (113 targets labeled) (**b**), and Sentinel-1 (331 targets labeled) (**c**) products in the Adriatic region.
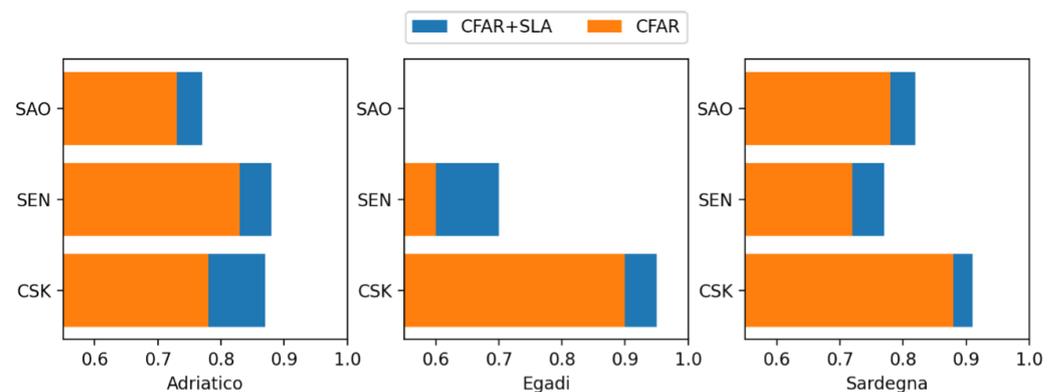

Figure 13. Comparative analysis of improved performance in terms of AUC for the considered sensors and the selected scenarios. CSK = COSMO-SkyMed, SAO = SAOCOM, and SEN = Sentinel-1.

5. Conclusions

Within the time frame of 18 months, the present study assessed the capability of a cascade detector for ship detection purposes on multiple SAR frequency bands (L-, C-, and X-bands). The processing chains and the constructed dataset of MM/MF SLC SAR products constitute an important contribution of this work. The results attained have confirmed the effectiveness of the developed approach, showing an increase in performance in terms of improvement of the AUC and reduction of false alarms. Indeed, in a very congested scenario, such as the port of Taranto, the reduction of the false alarm rate was estimated to be about 40%.

While undoubtedly recognizing the ghost targets, it must be pointed out that SLA involves the solution of an eigenvalue problem which is computationally intensive, with an increase in processing time that grows quadratically with the dimension of the considered tile. It should be taken into account how the time demanded by the discrimination phase matches the one from pre-selection. Therefore, to reduce the time required to process a panoramic SAR product, further research will analyze the capabilities offered by a deep learning-based technique on the developed dataset. Taking full advantage of the SAR spectrum is definitely a path that must be exploited with artificial intelligence.

Author Contributions: Conceptualization, A.R. and M.D.G.; methodology, R.D.P.; software, R.D.P.; validation, M.D.G., A.R.; formal analysis, R.D.P.; investigation, R.D.P.; resources, A.R. and M.D.G.; data curation, R.D.P.; writing—original draft preparation, R.D.P.; writing—review and editing, R.D.P., A.R. and M.D.G.; visualization, R.D.P.; supervision, A.R.; project administration, A.R.; funding acquisition, M.D.G. All authors have read and agreed to the published version of the manuscript.

Institutional Review Board Statement: Not applicable.

Informed Consent Statement: Not applicable.

Data Availability Statement: Due to confidentiality concerns and privacy regulations, the data used in this study cannot be distributed publicly.

Conflicts of Interest: The authors declare no conflict of interest.

References

1. Marghany, M. *Nonlinear Ocean Dynamics: Synthetic Aperture Radar*; Elsevier: Amsterdam, The Netherlands, 2021.
2. Graziano, M.D.; D'Errico, M.; Rufino, G. Wake component detection in X-band SAR images for ship heading and velocity estimation. *Remote Sens.* **2016**, *8*, 498. [CrossRef]
3. Graziano, M.D.; D'Errico, M.; Rufino, G. Ship heading and velocity analysis by wake detection in SAR images. *Acta Astronaut.* **2016**, *128*, 72–82. [CrossRef]
4. Graziano, M.D. Preliminary results of ship detection technique by wake pattern recognition in SAR images. *Remote Sens.* **2020**, *12*, 2869. [CrossRef]
5. Del Prete, R.; Graziano, M.D.; Renga, A. First results on wake detection in SAR images by deep learning. *Remote Sens.* **2021**, *13*, 4573. [CrossRef]
6. Vachon, P.W.; Campbell, J.; Bjerkelund, C.; Dobson, F.; Rey, M. Ship detection by the RADARSAT SAR: Validation of detection model predictions. *Can. J. Remote Sens.* **1997**, *23*, 48–59. [CrossRef]
7. Joshi, S.K.; Baumgartner, S.V. Range-Doppler tracking of ships using single-channel airborne radar data. In Proceedings of the EUSAR 2021; 13th European Conference on Synthetic Aperture Radar, VDE Conference, online, 29 March–1 April 2021; pp. 1–6.
8. Eldhuset, K. An automatic ship and ship wake detection system for spaceborne SAR images in coastal regions. *IEEE Trans. Geosci. Remote Sens.* **1996**, *34*, 1010–1019. [CrossRef]
9. Shao, Z.; Wu, W.; Wang, Z.; Du, W.; Li, C. Seaships: A large-scale precisely annotated dataset for ship detection. *IEEE Trans. Multimed.* **2018**, *20*, 2593–2604. [CrossRef]
10. Young, W. What are vessel traffic services, and what can they really do? *Navigation* **1994**, *41*, 31–56. [CrossRef]
11. Goudossis, A.; Katsikas, S.K. Towards a secure automatic identification system (AIS). *J. Mar. Sci. Technol.* **2019**, *24*, 410–423. [CrossRef]
12. Tetreault, B. Use of the Automatic Identification System (AIS) for maritime domain awareness (MDA). In Proceedings of the OCEANS 2005 MTS/IEEE, Washington, DC, USA, 19–23 September 2005; Volume 2, pp. 1590–1594. [CrossRef]
13. International Maritime Organization. "AIS transponders", International Maritime Organization (2017) [Online]. 2019. Available online: https://www.imo.org/en/OurWork/Safety/Pages/AIS.aspx (accessed on 7 December 2022).
14. Zhang, D.; Li, J.; Wu, Q.; Liu, X.; Chu, X.; He, W. Enhance the AIS data availability by screening and interpolation. In Proceedings of the 2017 4th International Conference on Transportation Information and Safety (ICTIS), Banff, AB, Canada, 8–10 August 2017; pp. 981–986.
15. Graziano, M.D.; Renga, A.; Moccia, A. Integration of Automatic Identification System (AIS) Data and Single-Channel Synthetic Aperture Radar (SAR) Images by SAR-Based Ship Velocity Estimation for Maritime Situational Awareness. *Remote Sens.* **2019**, *11*, 2196. [CrossRef]

16. Kanjir, U.; Greidanus, H.; Oštir, K. Vessel detection and classification from spaceborne optical images: A literature survey. *Remote Sens. Environ.* **2018**, *207*, 1–26. [CrossRef] [PubMed]

17. Iceye. Dark Vessel Detection for Maritime Security with SAR Data, [Online]. 2021. Available online: https://www.iceye.com/use-cases/security/dark-vessel-detection/interactive-demo (accessed on 8 March 2023).

18. Curlander, J.C.; McDonough, R.N. *Synthetic Aperture Radar*; Wiley: New York, NY, USA, 1991; Volume 11.

19. Wackerman, C.C.; Friedman, K.S.; Pichel, W.G.; Clemente-Colón, P.; Li, X. Automatic detection of ships in RADARSAT-1 SAR imagery. *Can. J. Remote Sens.* **2001**, *27*, 568–577. [CrossRef]

20. Friedman, K.; Wackerman, C.; Funk, F.; Rowell, K.; Pichel, W.; Clemente-Colón, P.; Li, X. Validation of an automatic vessel detection algorithm using SAR data and known vessel fleet distributions. In Proceedings of the IGARSS 2000. IEEE 2000 International Geoscience and Remote Sensing Symposium. Taking the Pulse of the Planet: The Role of Remote Sensing in Managing the Environment. Proceedings (Cat. No. 00CH37120), Honolulu, HI, USA, 24–28 July 2000; IEEE: New York, NY, USA, 2000 ; Volume 5, pp. 2071–2073.

21. Friedman, K.S.; Wackerman, C.; Funk, F.; Schwenzfeier, M.; Pichel, W.G.; Colon-Clemente, P.; Li, X. Analyzing the dependence between RADARSAT-1 vessel detection and vessel heading using CFAR algorithm for use on fishery management. In Proceedings of the Oceans 2003. Celebrating the Past... Teaming Toward the Future (IEEE Cat. No. 03CH37492), San Diego, CA, USA, 22–26 September 2003 ; Volume 5, pp. P2819–P2823.

22. Friedman, K.S.; Wackerman, C.; Funk, F.; Pichel, W.G.; Clemente-Colón, P.; Li, X. Validation of a CFAR vessel detection algorithm using known vessel locations. In Proceedings of the IGARSS 2001. Scanning the Present and Resolving the Future, Proceedings. IEEE 2001 International Geoscience and Remote Sensing Symposium (Cat. No. 01CH37217), Sydney, Australia, 9–13 July 2001; Volume 4, pp. 1804–1806.

23. Renga, A.; Graziano, M.D.; Moccia, A. Segmentation of marine SAR images by sublook analysis and application to sea traffic monitoring. *IEEE Trans. Geosci. Remote Sens.* **2018**, *57*, 1463–1477. [CrossRef]

24. Guarnieri, A.M. Adaptive removal of azimuth ambiguities in SAR images. *IEEE Trans. Geosci. Remote Sens.* **2005**, *43*, 625–633. [CrossRef]

25. Choi, J.H.; Won, J.S. Efficient SAR Azimuth Ambiguity Reduction in Coastal Waters Using a Simple Rotation Matrix: The Case Study of the Northern Coast of Jeju Island. *Remote Sens.* **2021**, *13*, 4865. [CrossRef]

26. Velotto, D.; Soccorsi, M.; Lehner, S. Azimuth ambiguities removal for ship detection using full polarimetric X-band SAR data. *IEEE Trans. Geosci. Remote Sens.* **2013**, *52*, 76–88. [CrossRef]

27. Pelich, R.; Longépé, N.; Mercier, G.; Hajduch, G.; Garello, R. AIS-based evaluation of target detectors and SAR sensors characteristics for maritime surveillance. *IEEE J. Sel. Top. Appl. Earth Obs. Remote Sens.* **2014**, *8*, 3892–3901. [CrossRef]

28. Wang, C.; Bi, F.; Zhang, W.; Chen, L. An intensity-space domain CFAR method for ship detection in HR SAR images. *IEEE Geosci. Remote Sens. Lett.* **2017**, *14*, 529–533. [CrossRef]

29. Raney, R.K.; Princz, G.J. Reconsideration of azimuth ambiguities in SAR. *IEEE Trans. Geosci. Remote Sens.* **1987**, *GE-25*, 783–787. [CrossRef]

30. Touzi, R.; Hurley, J.; Vachon, P.W. Optimization of the degree of polarization for enhanced ship detection using polarimetric RADARSAT-2. *IEEE Trans. Geosci. Remote Sens.* **2015**, *53*, 5403–5424. [CrossRef]

31. Touzi, R. On the use of polarimetric SAR data for ship detection. In Proceedings of the IEEE 1999 International Geoscience and Remote Sensing Symposium. IGARSS'99 (Cat. No. 99CH36293), Hamburg, Germany, 28 June–2 July 1999 ; Volume 2, pp. 812–814.

32. Brekke, C.; Anfinsen, S.N. Ship detection in ice-infested waters based on dual-polarization SAR imagery. *IEEE Geosci. Remote Sens. Lett.* **2010**, *8*, 391–395. [CrossRef]

33. Marino, A.; Sanjuan-Ferrer, M.J.; Hajnsek, I.; Ouchi, K. Ship detection with spectral analysis of synthetic aperture radar: A comparison of new and well-known algorithms. *Remote Sens.* **2015**, *7*, 5416–5439. [CrossRef]

34. Wang, W.; Ji, Y.; Lin, X. A novel fusion-based ship detection method from Pol-SAR images. *Sensors* **2015**, *15*, 25072–25089. [CrossRef]

35. Xie, Q.; Ballester-Berman, J.D.; Lopez-Sanchez, J.M.; Zhu, J.; Wang, C. Quantitative analysis of polarimetric model-based decomposition methods. *Remote Sens.* **2016**, *8*, 977. [CrossRef]

36. Zhu, J.; Qiu, X.; Pan, Z.; Zhang, Y.; Lei, B. Projection shape template-based ship target recognition in TerraSAR-X images. *IEEE Geosci. Remote Sens. Lett.* **2016**, *14*, 222–226. [CrossRef]

37. Wang, C.; Bi, F.; Chen, L.; Chen, J. A novel threshold template algorithm for ship detection in high-resolution SAR images. In Proceedings of the 2016 IEEE International Geoscience and Remote Sensing Symposium (IGARSS), Beijing, China, 10–15 July 2016 ; pp. 100–103.

38. Song, S.; Xu, B.; Yang, J. SAR target recognition via supervised discriminative dictionary learning and sparse representation of the SAR-HOG feature. *Remote Sens.* **2016**, *8*, 683. [CrossRef]

39. Zhou, D.; Zeng, L.; Zhang, K. A novel SAR target detection algorithm via multi-scale SIFT features. *J. Northwest. Polytech. Univ.* **2015**, *33*, 867–873.

40. Ai, J.; Tian, R.; Luo, Q.; Jin, J.; Tang, B. Multi-scale rotation-invariant Haar-like feature integrated CNN-based ship detection algorithm of multiple-target environment in SAR imagery. *IEEE Trans. Geosci. Remote Sens.* **2019**, *57*, 10070–10087. [CrossRef]

41.	Zhang, T.; Zhang, X. High-speed ship detection in SAR images based on a grid convolutional neural network. *Remote Sens.* **2019**, *11*, 1206. [CrossRef]

42.	Chen, C.; He, C.; Hu, C.; Pei, H.; Jiao, L. A deep neural network based on an attention mechanism for SAR ship detection in multiscale and complex scenarios. *IEEE Access* **2019**, *7*, 104848–104863. [CrossRef]

43.	Zhang, T.; Zhang, X.; Shi, J.; Wei, S. Depthwise separable convolution neural network for high-speed SAR ship detection. *Remote Sens.* **2019**, *11*, 2483. [CrossRef]

44.	Wang, Y.; Wang, C.; Zhang, H.; Dong, Y.; Wei, S. A SAR dataset of ship detection for deep learning under complex backgrounds. *Remote Sens.* **2019**, *11*, 765. [CrossRef]

45.	Chang, Y.L.; Anagaw, A.; Chang, L.; Wang, Y.C.; Hsiao, C.Y.; Lee, W.H. Ship detection based on YOLOv2 for SAR imagery. *Remote Sens.* **2019**, *11*, 786. [CrossRef]

46.	Jiao, J.; Zhang, Y.; Sun, H.; Yang, X.; Gao, X.; Hong, W.; Fu, K.; Sun, X. A densely connected end-to-end neural network for multiscale and multiscene SAR ship detection. *IEEE Access* **2018**, *6*, 20881–20892. [CrossRef]

47.	Li, J.; Qu, C.; Shao, J. Ship detection in SAR images based on an improved faster R-CNN. In Proceedings of the 2017 SAR in Big Data Era: Models, Methods and Applications (BIGSARDATA), Beijing, China, 13–14 November 2017 ; pp. 1–6.

48.	Wei, S.; Zeng, X.; Qu, Q.; Wang, M.; Su, H.; Shi, J. HRSID: A high-resolution SAR images dataset for ship detection and instance segmentation. *IEEE Access* **2020**, *8*, 120234–120254. [CrossRef]

49.	Colin, A.; Fablet, R.; Tandeo, P.; Husson, R.; Peureux, C.; Longépé, N.; Mouche, A. Semantic segmentation of metoceanic processes using SAR observations and deep learning. *Remote Sens.* **2022**, *14*, 851. [CrossRef]

50.	Biffia, A.; Dodaro, L.; Morabito, F.; Pergolizzi, A. Mare Monstrum. 2020. Available online: https://www.legambiente.it/wp-content/uploads/Dossier-Mare-Monstrum-2019.pdf (accessed on 13 December 2022).

51.	Biffia, A.; Dodaro, L.; Morabito, F.; Pergolizzi, A. Mare Monstrum. 2019. Available online: https://www.legambiente.it/wp-content/uploads/2020/06/MareMonstrum2020.pdf (accessed on 13 December 2022).

52.	Furesi, R.; Madau, F.; Pulina, P.; Sai, R.; Pinna, M.; Pais, A. Profitability and sustainability of edible sea urchin fishery in Sardinia (Italy). *J. Coast. Conserv.* **2016**, *20*, 299–306. [CrossRef]

53.	Spera, G.; Monaco, P. Rapporto Annuale sul Controllo Della Pesca in Italia. 2019. Available online: https://www.guardiacostiera.gov.it/stampa/Documents/RAPPORTO%20ANNUALE%202020%20-%20DOWNLOAD.pdf (accessed on 13 December 2022).

54.	Graziano, M.D.; Prete, R.D.; Grasso, M. A New Dataset of Multi-Mission/multi-Frequency sar Data for Maritime Monitoring: First Results and Critical Analysis. 2022. Available online: https://iafastro.directory/iac/paper/id/74577/summary/ (accessed on 13 December 2022).

55.	Miler, R.K. The Exactearth Satelite-AIS Benefits for the Maritime Transport. *Prace Naukowe Wyższej Szkoły Bankowej w Gdańsku* **2013**, *28*, 71–86.

56.	Dellepiane, S.; De Laurentiis, R.; Giordano, F. Coastline extraction from SAR images and a method for the evaluation of the coastline precision. *Pattern Recognit. Lett.* **2004**, *25*, 1461–1470. [CrossRef]

57.	Open Street Map. "Data Derived from OpenStreetMap for Download", Open Street Map [Online]. 2022. Available online: https://osmdata.openstreetmap.de/data/land-polygons.html (accessed on 7 December 2022).

58.	Benachenhou, K.; Taleb-Ahmed, A.; Hamadouche, M. Performances evaluation of GNSS ALTBOC acquisition with CFAR detection in Rayleigh fading channel. In Proceedings of the 2013 Saudi International Electronics, Communications and Photonics Conference, Riyadh, Saudi Arabia, 27–30 April 2013; pp. 1–7.

59.	Guida, M.; Longo, M.; Lops, M. Biparametric CFAR procedures for lognormal clutter. *IEEE Trans. Aerosp. Electron. Syst.* **1993**, *29*, 798–809. [CrossRef]

60.	Anastassopoulos, V.; Lampropoulos, G.A. Optimal CFAR detection in Weibull clutter. *IEEE Trans. Aerosp. Electron. Syst.* **1995**, *31*, 52–64. [CrossRef]

61.	Erfanian, S.; Vakili, V.T. Introducing excision switching-CFAR in K distributed sea clutter. *Signal Process.* **2009**, *89*, 1023–1031. [CrossRef]

62.	Leng, X.; Ji, K.; Yang, K.; Zou, H. A Bilateral CFAR Algorithm for Ship Detection in SAR Images. *IEEE Geosci. Remote Sens. Lett.* **2015**, *12*, 1536–1540. [CrossRef]